On the equilibrium electrostatic potential and light-induced charge redistribution under illumination in halide perovskite structures

Davide Regaldo[a,b,c], Aleksandra Bojar[a,b,c], Sean P. Dunfield[d,e], Pilar Lopez-Varo[a], Mathieu Frégnaux[a,f], Vincent Dufoulon[a,g], Shan-Ting Zhang[a], José Alvarez[a,b,c], Joseph J. Berry[d], Jean-Baptiste Puel[a,h], Philip Schulz[a,g], Jean-Paul Kleider[a,b,c].

[a] IPVF, Institut Photovoltaïque d'Ile-de-France, 18, Boulevard Thomas Gobert, 91120 Palaiseau France; [b] Université Paris-Saclay, CentraleSupélec, CNRS, Laboratoire de Génie Electrique et Electronique de Paris, 91192, Gif-sur-Yvette, France; [c] Sorbonne Université, CNRS, Laboratoire de Génie Electrique et Electronique de Paris, 75252, Paris, France, [d] National Renewable Energy Laboratory, 15013 Denver West Pkwy, Golden, CO 804011;[e] Materials Science & Engineering Program, 027 UCB, University of Colorado Boulder, Boulder, CO 803032;[f] Institut Lavoisier de Versailles, Université de Versailles Saint-Quentin-en-Yvelines, Université Paris-Saclay, CNRS, UMR 8180, 45 avenue des Etats-Unis, 78035 Versailles Cedex, France7; [g] CNRS, École Polytechnique, IPVF, UMR 9006, 18, Boulevard Thomas Gobert, 91120 Palaiseau, France; [h] EDF R&D, 91120 Palaiseau, France;

Lead halide perovskites are a class of semiconductor materials which are employed as non-intentionally doped absorbers inserted between two selective carrier transport layers (SCTL), realizing a p-i-n or n-i-p heterojunction. In our study, we have developed and investigated a lateral device, based on methylammonium lead iodide ($MAPbI_3$) in which the p-i-n heterojunction develops in the horizontal direction. Our research suggests that the effective doping level in the $MAPbI_3$ film should be very low, below 10^{12} cm^{-3}. Along the vertical direction, this doping level is not enough to screen the electric field of the buried heterojunction with the SCTL. The perovskite work function is therefore affected by the work function of the SCTL underneath. From drift-diffusion simulations we show that intrinsic perovskite-SCTL structures develop mV range surface photovoltages (SPVs) under continuous illumination. However, perovskite-SCTL structures can develop SPVs of hundreds of mV, as confirmed by our measurements. We therefore analyzed the compatibility between low doping and low defect densities in the perovskite layer and such high SPV values using numerical modelling. It is shown that these high SPV

values could originate from electronic processes due to large band offsets in the buried perovskite-SCTL heterojunctions, or at the SCTL - transparent conductive oxide (TCO) buried heterojunction. However, such electronic processes can hardly explain the long SPV persistence after switching off the illumination.

Keywords: Perovskite solar cell, surface photovoltage, heterojunction, drift-diffusion modelling, photoemission spectroscopy, defects.

1 | INTRODUCTION

Metal halide perovskite (MHP) solar cells (PSC) have experienced a rapid increase in efficiency in the last decade. The quality of the perovskite absorber (e.g. high absorption coefficient, low recombination and high diffusion length in the domain of polycrystalline materials) and of the heterointerfaces (selectivity by carrier-blocking band offsets, low interface recombination, transparency of the selective carrier transport layers (SCTLs)) are considered as key factors for the high power-conversion efficiency (PCE) achieved [1][2].

However, despite the record improvements in power conversion efficiency (PCE) of PSCs, the community still faces an ongoing debate about the nature and concentration of defects in the absorber layer. Several studies report the presence of native defects in MHPs, which are dependent on the MHP deposition process [3]. Moreover, upon external stimuli, such as illumination, an oxidizing or reducing environment, or a bias voltage, defects could be created or destroyed [4]

[5].

Polycrystalline MHP thin films show defects both in bulk and on the grain boundaries [6]. In addition, material stability improvements have not kept pace with the PCE increase, mainly due to the many novel properties of this material, like its ionic organic-inorganic structure. Related to the crystal lattice properties, the perovskite's shallow defect levels have very low formation energies and could induce a nonzero doping level in the material[6][7].

Direct measurements of the doping level in perovskites, like capacitance-voltage profiling, still depict a major challenge. Perovskites are generally chemically reactive when brought in contact with a wide variety of metals [8]. In addition, capacitance techniques rely on the presence of a defined space charge region, a condition which is difficult to achieve for lowly doped and thin (sub-micron) semiconducting layers [9].

X-ray and ultraviolet photoemission spectroscopy (XPS, UPS) have been employed to characterize electronic and chemical properties of the perovskite material [10]. Furthermore, transient surface photovoltage (SPV) measurements in fixed capacitor configuration, Kelvin probe and Kelvin probe force microscopy (KPFM) have been employed to measure the charge extraction capabilities of perovskite - SCTL structures[11][12].

In several past studies, a combination of these techniques revealed that the Fermi level position in the bandgap of the perovskite can be changed by interfacing the MHP layer with different substrates[13][14][15][16]. However, to date the exact origin of this effect remains unresolved and could be rooted in subtle chemical interactions between the perovskite film and substrate. This supposed variability, together with the effect of different deposition techniques, produces a very complex system, loosely described by the term “p-i-n heterojunction”.

In conventional, vertically stacked n-i-p or p-i-n solar cells, the absorber is sandwiched between the SCTLs. Therefore, only indirect measurements can be employed to study the impact of the SCTL on the electronic properties of the junction. In this work, we used a lateral solar cell layout, similar to the design of interdigitated back contact solar cells (IBC). The two SCTLs were deposited prior to the perovskite layer, thus forming two buried heterojunctions. In this way, the absorber properties can be measured with surface sensitive techniques and the contribution of each buried heterojunction can be separated by making the channel between the two SCTLs large enough to contain micrometric space charge regions (SCRs).

Here, we employed XPS, UPS, and KPFM techniques in order to acquire chemical or electronic information about the materials and their mutual interactions. XPS and UPS techniques allow us to probe the equilibrium electrostatic potential distribution across the channel between the two SCTLs. From KPFM measurements performed both in the dark and under illumination we obtain local SPV values that depend on the charge redistribution and thus on their extraction/injection

ability at the perovskite-SCTL heterointerfaces. Experimental data are interpreted using a full 3D finite-element modeling tool in order to build a comprehensive energy diagram analysis and get insights into perovskite material parameters related to defect and doping properties.

2 |Results and discussion

2.1 | XPS scan mode surface potential analysis

We consider the perovskite lateral heterojunction device described in Figure 2a. It is composed of an FTO substrate on which two SCTLs, namely TiO_x and NiO_x, which act as electron transport layer (ETL) and hole transport layer (HTL), respectively, were deposited and laser scribed in order to create a channel between them ($l_{ch} > 50$ µm). Then, a $MAPbI_3$ perovskite layer was deposited on top, leaving the surface available for characterization and illumination.

The structures were previously characterized using different techniques [17]. We focus here on the XPS, UPS, KPFM and SPV techniques and on modelling the experimental data to derive conclusions regarding the doping and defects in the perovskite material as well as the impact of the SCTLs on the energy profiles and carrier distributions in the dark and under illumination.

We employed XPS both in scanning and imaging mode. The first of these two methods allowed us to acquire the signal rapidly, minimizing the possible radiation damage during measurement, with a total measurement time of 30 minutes. In this acquisition mode, we swept the probed area across the channel (illustrated in Figure 2a) and performed local XPS measurements. We measured the variation across the channel of the $I_{3d_{5/2}}$ core level peak energy, BE_I, which is representative of the electrostatic potential variation, as shown in Figure 1.

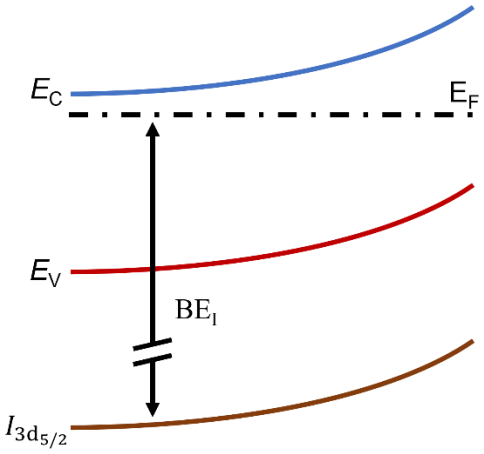

Figure 1: Sketch of the $I_{3d_{5/2}}$ core level, top of the valence band, E_V, and bottom of the conduction band, E_C, in presence of a space-dependent electrostatic potential, $q\varphi(x) = BE_I(x) = E_F - I_{3d_{\frac{5}{2}}}(x)$.

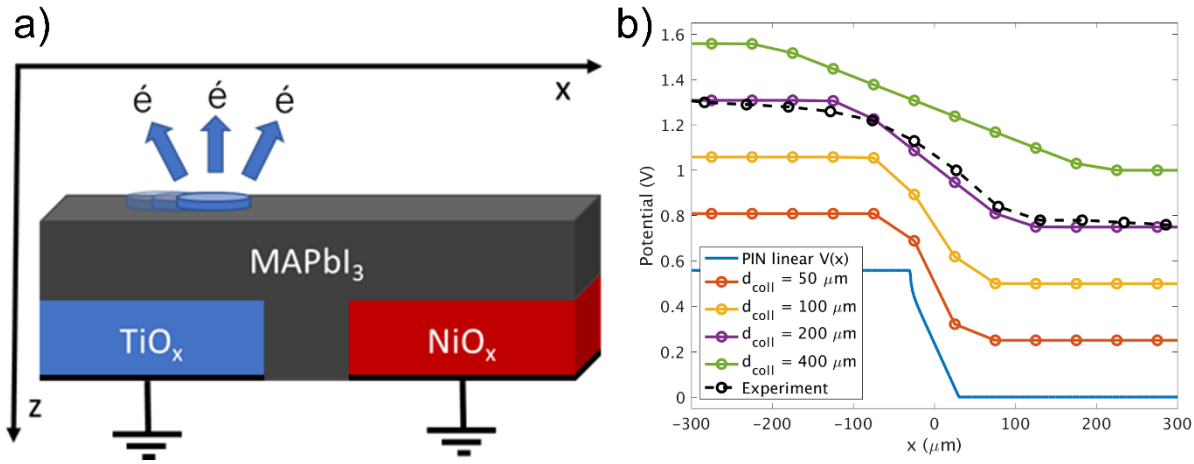

Figure 2: sketch of the LHJ device with the representation of the XPS electron collection area in the scanning mode (a). In (b) the apparent surface electrostatic potential profile across the channel obtained from XPS experimental data (black dashed line) is compared to the one calculated from modelling using an intrinsic perovskite, under various electron collection diameters (d_{coll}). The blue solid line shows the calculated surface potential profile without convolution effect with the probe area (also corresponding to d_{coll}=0). The reference for the electrostatic potential (0 V) is taken on top of the NiO_x side and the origin of the x axis is taken in the middle of the channel. Curves have been shifted with respect to each other for clarity.

XPS scanning data show that a perceived gradual potential drop is present across the channel [17] (Figure 2b black dashed line).

In this scanning XPS mode, each measured point is the average value of the collected electrons arriving from a given probe area. Therefore, to have a true comparison with the experiments, the surface electrostatic potential values calculated from modeling have been averaged over a simulated collection distance d_{coll}, that we varied between 50 µm and 400 µm. Input material

parameters for the modelling are reported in Table S2. In Fig. 2b we compare the corresponding apparent surface potential profiles to the XPS experimental data (dark dashed line) and to the true calculated surface potential profile (blue curve without symbols). On the regions above the HTL and the ETL, far from the channel location, the potential is constant. The linear voltage drop in the channel is due to the perovskite being considered undoped and defect-free. A high-curvature electron accumulation region is visible closer to the TiO_x side, being the perovskite over the ETL moderately n-type ($E_F - E_V = 1.31$ eV). Such a high curvature region is not present on the HTL side due to the perovskite being almost intrinsic above NiO_x (Table S1). Convoluting the surface potential with the collection area of the XPS setup shows that, when the area increases, the slope of the surface potential decreases, while the perceived channel length increases. We here emphasize that a good agreement is found between the experimental data and the apparent surface potential profile calculated with a collection diameter of 200 µm, which corresponds to the value in our experimental XPS scan mode. However, the perovskite was assumed to be undoped and we thus need to study how doping and defects affect the surface potential variation and the corresponding apparent variation obtained from the XPS scan with the 200 µm collection diameter. We thus added a trap level in the bandgap close to the band edge. It was considered as an acceptor ($E_{tA} - E_V$=0.02 eV) or as a donor ($E_C - E_{td}$ = 0.02 eV) in order to induce p or n-type doping, respectively [7]. Trap parameters are summarized in Table S2. In a first example, we chose low bulk trap densities (10^{13} cm^{-3}). As shown in Figure S3a-c, these low densities are large enough to create two separate SCRs in the channel, while leaving a nearly flat potential region in the middle. Due to the $E_F - E_V$ values at the two extremes, introducing a light effective n-type doping pins the channel potential to a value between the two extremes. However, this shift remains undetectable to the measurement probe due to the large collection area. On the other hand, an effective p-type doping causes a larger shift of the potential towards more negative values, which results in a significant deviation from the experimental gradual potential drop.

Therefore, Figure S3 shows that the resolution of the measurement allows to classify the perovskite to be intrinsic or lightly n-type, and to rule out the presence of moderate or high p-type doping.

We simulated the surface potential across the channel for various trap concentrations in the bulk perovskite (Figure S5a) and convoluted the data with the experimental electron collection area (d_{coll} = 200 µm), as shown in Figure 3. As the trap density increases, the potential drifts away from the linear trend, towards a parabolic-like shape, leading to Fermi level pinning inside the channel.

Values of donor trap density up to 10^{15}cm^{-3} produce no effect on the apparent surface potential derived from XPS due to the convolution of the actual potential with the XPS collection area. Higher donor trap densities are able to screen the buried heterojunction in the vertical direction, which leads to a constant surface potential across the channel. This is confirmed by the vertical perovskite - NiO_x band diagram (Figure S5b), and by an analytical model. Indeed, considering an n-type doped perovskite – p-type doped HTL structure, we can employ the full depletion approximation and consider the HTL as a metal contact. In this case, assuming a certain perovskite relative permittivity variability ($5 < \varepsilon_r < 50$), the minimum perovskite doping density necessary to vertically screen the buried heterojunction is 10^{15}cm^{-3} (see the modelling section for a more complete analysis).

On the other hand, we find that acceptor trap densities higher than 10^{12} cm^{-3} are not compatible with the experimental findings, as they would modify the gradual potential drop as shown in Figure 3.

Therefore, XPS measurements in scanning mode allow us to classify the perovskite to be intrinsic or slightly n-type, with effective doping concentration up to 10^{15}cm^{-3}, and to rule out the presence of p-type effective doping with concentrations larger than 10^{12}cm^{-3}.

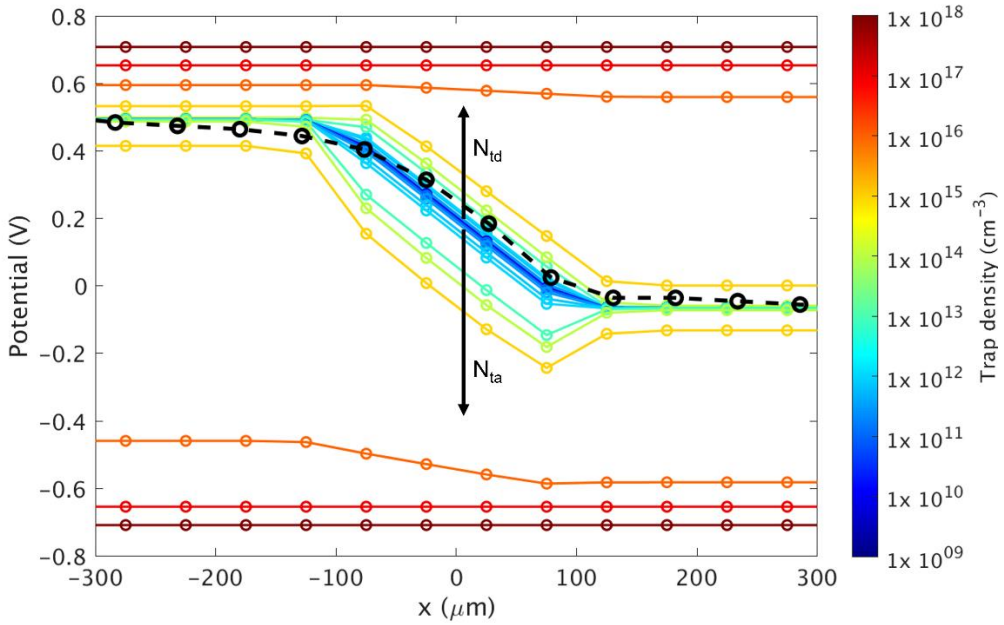

Figure 3: Surface potential of the $MAPbI_3$ perovskite across the LHJ device convoluted with the 200 μm collection diameter of the XPS setup employed, for different trap (shallow donor N_{td} or shallow acceptor N_{ta}) concentrations in the perovskite. The dark dashed line represents the experimental data.

In addition to the XPS scanning mode technique, we used the XPS imaging mode on a 500 x 500 μm^2 region of the LHJ device which overlays the channel area with a spatial resolution up to 5 μm. The XPS imaging mode data show, in accordance with the XPS scanning mode, a surface potential difference of ~ 500 mV between the two sides of the LHJ. In addition, a linear potential variation can be seen in a 60 μm wide region, that corresponds to the length of the LHJ channel (see SI for the detailed analysis).

Finally, we added donor traps on the surface of the perovskite, in a concentration of 10^9 cm^{-2}, as shown in Figure S3b. This trap density is able to pin the channel potential in a value between the two extremes, similarly to bulk donor traps in Figure S3a.

While perovskite p-type doping character larger than 10^{12} cm^{-3} had already been excluded by the analysis of the XPS scanning data, the linear voltage drop across a ~ 60 μm region recorded by high-resolution imaging allows us to further confine the range of possible doping densities. According to the depletion region considerations, we can also set the upper limit for n-type doping

in the perovskite to 10^{12} cm^{-3}, since larger doping values would have laterally screened the HTL - perovskite heterojunction.

2.2 |KPFM surface photovoltage analysis

To gain more insight into the materials properties and the charge redistribution upon illumination, we used KPFM measurements in the dark and under illumination. From the contact potential difference (CPD) between the sample surface and the tip measured by KPFM in dark equilibrium conditions we can deduce the surface work function of the sample. KPFM under variable bias or illumination measures the shift of the surface potential caused by an external stimulus. This shift depends upon the charge redistribution across the layer stack: it is therefore influenced by the presence of surface or bulk defects, or by electric fields present in surface or buried junctions and by band alignments at heterojunctions [11]. Specifically, by subtracting the CPD measured in the dark to that measured under illumination, one obtains the local surface photovoltage (SPV). Preliminary measurements on the $MAPbI_3$ perovskite LHJ device of Figure 2a were reported elsewhere

[*17*]. We observed a large positive SPV (≈ 500 mV) on top of TiO_x, and a smaller but negative SPV on top of NiO_x (≈ -320 mV). Here we want to extend the measurements and analysis to triple cation mixed halide perovskite layers over different transport layers. We thus fabricated perovskite-SCTL structures employing a triple cation mixed halide perovskite and three different SCTLs: TiO_x, SnO_x and NiO_x (see SI). We characterized the bilayers with a KPFM setup, in which we illuminated the samples with a 532 nm laser centered on the KPFM tip. We also measured the surface work functions for all the materials under study employing a highly oriented pyrolytic graphite reference sample. We observed the perovskite work function (WF) dependence on the substrate, in line with literature reports [16] (Table 1).

	TCO WF	SCTL WF (fresh) (eV)	SCTL WF (aged) (eV)	Perovskite WF (fresh) (eV)
FTO/TiO_2 UVO	4.79	4.40	4.30	4.73
ITO/SnO_2 UVO	5.02	4.74	4.63	4.66
ITO/NiO_x UVO-A	5.02	5.06	4.87	5.09

Table 1: KPFM surface work function (WF) measurements for the materials under study (TCO - SCTL - perovskite layer stacks).

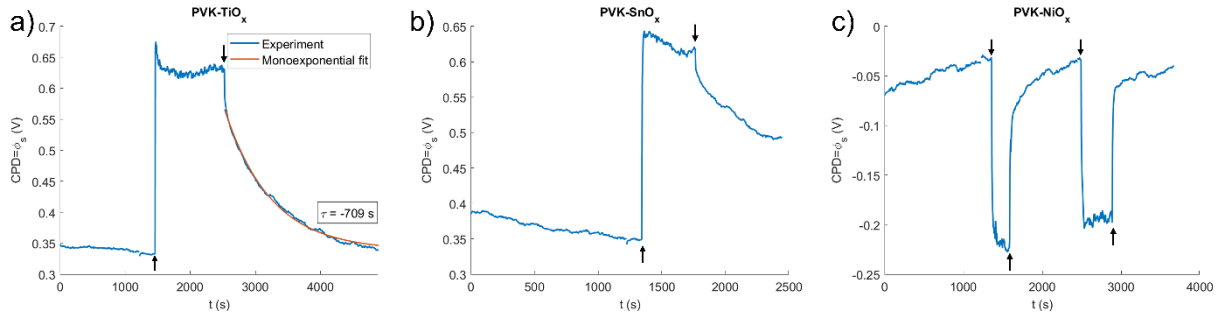

Figure 4: KPFM measurements performed on perovskite-SCTL structures, under 532 nm laser illumination. CPD measurement of (a) perovskite-TiO_x, (b) perovskite-SnO_x, and (c) perovskite-NiO_x. Arrows indicate switch on and subsequent switch off times of the 532 nm laser illumination.

KPFM measurements under illumination show that the sign of the surface photovoltage (SPV) is consistent with the nature of the SCTL underneath the perovskite, i.e. negative for the perovskite-HTL and positive for the perovskite-ETL structure (Figure 4), and it is reproducible (see Figure S9). This is comparable to our previous measurements on $MAPbI_3$. The sign of the respective SPVs can be attributed to charge separation at the perovskite-SCTL interface. Due to the accumulation of blocked carriers inside the perovskite, a net charge builds up and the surface potential shifts under illumination [18]. The amplitude of the SPV is on the order of 300 mV for the perovskite on both ETL layers, and 170 mV for the perovskite on NiO_x. Regarding the perovskite-TiO_x structure, SPVs of 150-200 mV have already been observed, while perovskite-HTL structures showed 2 orders of magnitude lower SPVs. This difference has been ascribed to a

higher efficiency of charge extraction at the perovskite-ETL interface, with respect to the perovskite-HTL one [11].

The timescales of the SPV buildup after switch-on and decay after switch-off are signatures of the processes involved in the SPV formation. In our case, the rise of the SPV upon switching on the illumination is at least three orders of magnitude faster than the decay of SPV after turning off the illumination, taking into account the low temporal resolution of the instrument (~4 s). In addition, for both transients after the switch-on and switch-off processes, we observe a fast component followed by a slower one. The instantaneous surface potential changes are summarized in Table 2.

	SPV fast buildup (V)	SPV fast decay (V)
FTO/TiO_x/Perovskite	0.32	0.04
ITO/SnO_x/Perovskite	0.22	0.03
ITO/NiO_x/ Perovskite	0.11	0.07

Table 2: Fast SPV component for the bilayers under study. The first column reports the instantaneous surface potential change when the sample is illuminated, while the second column refers to the instantaneous surface potential change when the illumination is switched off.

We also observe that the fast component after switch-off is very small and, for the perovskite-TiO_x sample, is followed by a slow monoexponential decrease with a characteristic time constant of about 700 s. (Figure 4a).

Due to the lack of analytical solutions to the Poisson and carrier continuity equations for many non-equilibrium and non-steady state conditions, we have employed drift-diffusion modelling to unveil the root causes of the SPV and study its dynamics under continuous monochromatic illumination in our perovskite - SCTL bilayers. For comparison with experimental data, we have

chosen the same light intensity employed in the KPFM measurements (~8 W/cm^2). Simulation parameters are listed in Table S3.

We start with the ideal case, in which the perovskite is intrinsic and without defects states in the bandgap, and the SCTL is also without defects states in the bandgap but doped ($N_{\mathrm{dop}} = 10^{17}\mathrm{cm}^{-3}$). In addition, we consider zero band offset between the perovskite and the SCTL for the type of carriers that should be extracted at this interface. At equilibrium, the perovskite being undoped and defect-free, the position of the Fermi level in the perovskite is imposed by the doped SCTL underneath, and only a low built-in voltage of about 100 mV forms across the heterojunction.

Under illumination, electrons and holes are separated at the heterointerface: holes accumulate in the perovskite, while electrons accumulate inside the ETL. The sign of the calculated SPV is therefore positive. The charge redistribution is opposite in the perovskite - HTL structure, where the sign is negative. Noticeably, the amplitude of the SPV in both types of structures is lower than 1 mV (Figure 5).

In conclusion, this simple modelling of the perovskite-ETL and perovskite-HTL structures cannot explain the large amplitudes that are experimentally observed. In addition, the calculated transients are much faster (Figure S8). We therefore studied which other factors could affect rise, decay time and magnitude of the SPV.

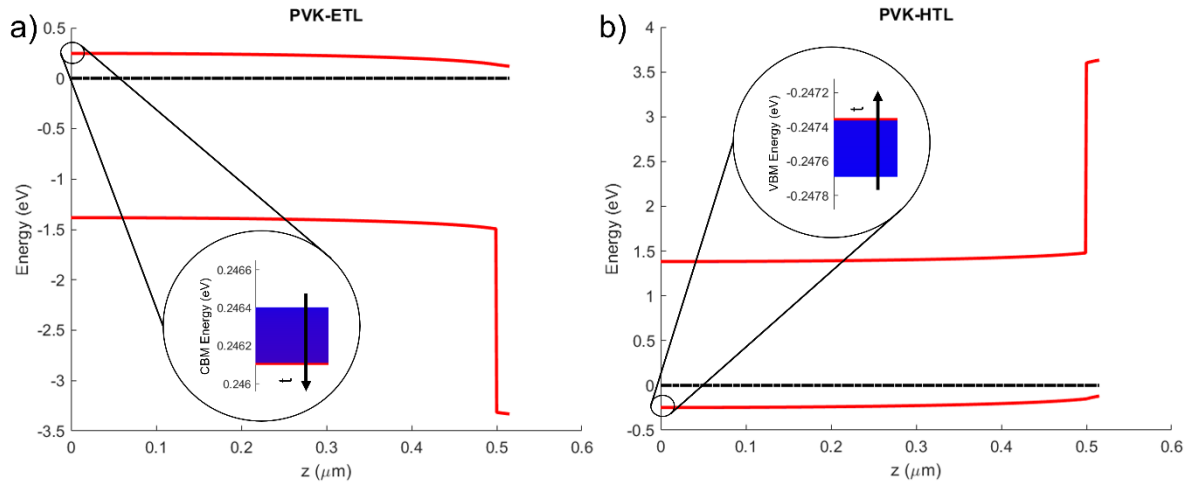

Figure 5: perovskite-ETL (a) and perovskite-HTL (b) band diagrams under illumination; the shift of the surface potential is visible in the insets (positive for PVK-ETL, negative for PVK-HTL).

P-type doping of the perovskite

A built-in voltage across a buried (hetero)junction is usually considered as a primary source of surface photovoltage formation. Regarding the perovskite - TiO_x structure, the presence of effective p-type doping in the perovskite could increase the magnitude of the built-in voltage of the heterojunction, since TiO_x has been considered as n-type (with a donor concentration $N_d = 10^{17}\,cm^{-3}$). Thus, an increase of the SPV under the same illumination conditions is expected. Results of the transient SPV curves for both switch-on and switch-off are displayed in Figure 6, showing that the magnitude of the SPV and corresponding decay times increase with the perovskite acceptor doping concentration.

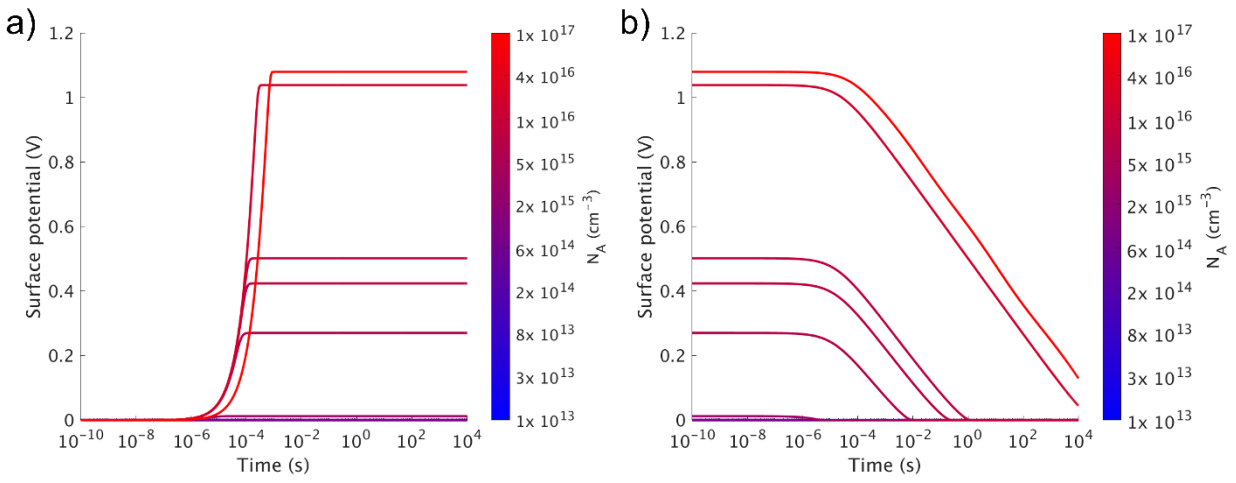

Figure 6: Perovskite - TiO_x transient SPV simulations for different values of acceptor dopant concentration in the perovskite; build-up of SPV after illumination is switched on (a), and SPV decay after illumination is switched off (b).

Perovskite doping values of $7x10^{15}$ cm^{-3} and $9x10^{15}$ cm^{-3} provide SPVs of 0.27 V and 0.42 V, respectively, which are comparable to the experimental value. In addition, KPFM measured the perovskite WF dependence on the SCTL WF. For the perovskite – TiO_x structure, $WF_{\mathrm{pvk}} - WF_{\mathrm{TiO_x}} \approx 0.4$ eV, which in equilibrium could indicate the presence of $5x10^{15}$ cm^{-3} acceptor dopants in the perovskite, as shown in Figure S10a. However, this heterostructure would develop only a 120 mV SPV, which is at least 100 mV lower than the one found in the experiment.

In addition, the characteristic decay time of the simulated SPV is considerably lower than the 700 s observed experimentally. We also note that the simulated transient after switch-off exhibits a non-exponential decay, in contrast with the exponential behavior observed experimentally for long times (Figure 4a). Therefore, possible p-type doping of the perovskite is unable to explain the experimental SPV results.

Band offset between perovskite and the transport layer

For selectivity purposes, large valence band offset at the ETL interface is preferable in order to prevent holes, generated in the perovskite, from diffusing into the ETL. At the same time the conduction band offset should be small in order to facilitate electron collection. Thus, the conduction band offset defined as the difference at the interface between the bottom of the conduction band in the perovskite, $E_{\mathrm{C,pvk}}$, and that in the TiO_x, $E_{\mathrm{C,TiO_x}}$, $\Delta E_C = E_{\mathrm{C,pvk}} - E_{\mathrm{C,TiO_x}}$, should ideally be close to zero. However, we found that a significantly positive value could be a source of large surface photovoltage, as depicted in Figure 7. Under illumination, electron-hole pairs are continuously generated inside the perovskite layer. In steady state conditions, however, the net flux of electrons across the perovskite - ETL heterojunction should be zero (open circuit conditions). For positive values of the conduction band offset, the electrons reinjected towards the perovskite from the TiO_x have to overcome a potential barrier in a thermionic emission process. If

the barrier height increases, the net amount of electrons accumulated in the TiO_x layer has to increase, in order to keep a net zero flux of electrons in steady state. This leads to the building of a net positive charge in the perovskite, which shifts the surface potential towards more positive values.

The same reasoning would be valid for a perovskite - HTL structure with opposite values of the valence band offset with respect to the ones shown in Figure 7.

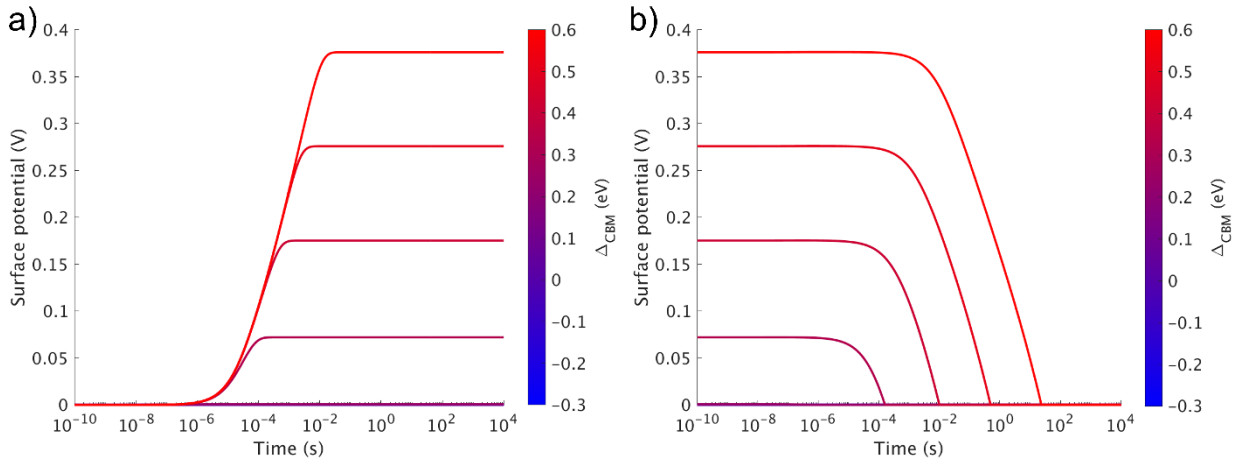

Figure 7: Perovskite - TiO_x transient SPV simulations for different values of conduction band offset. $\Delta E_C = E_{C,pvk} - E_{C,TiO_x}$; build-up of SPV after illumination is switched on (a), and SPV decay after illumination is switched off (b)

Conduction band offsets of 0.5 and 0.6 eV provide SPVs of 0.28 and 0.38 V, respectively, which are comparable to the experimental values. However, the characteristic decay time of the SPV related to this process is again considerably lower than experimentally observed, and the simulated transient at switch-off is non-exponential. In addition, we expect that such large values of conduction band offset would limit the efficiency of solar cells. In conclusion, the experimental SPV amplitude and transients cannot be explained solely by the conduction band offset at the perovskite-SCTL heterojunction.

Defects in the SCTL

So far, we have considered the SCTLs to be crystalline and moderately doped with no bandgap defects. However, these materials are generally polycrystalline and, especially for NiO_x, TiO_x and

SnO_x, not - intentionally doped. Therefore, it is not foregone that these materials possess a high dopant - defect ratio. In addition, the presence of a surface depletion region in polycrystalline oxides has already been reported [19][20]. If acceptor traps are present inside an ETL, under illumination they could trap photogenerated electrons which are injected from the perovskite thanks to the favorable conduction band alignment. However, in order to capture electrons and change the trap occupation, their energy level must lie above the Fermi level at equilibrium.

We found that the only way to significantly increase the SPV was to introduce such a large acceptor trap density at the surface of the ETL, that the Fermi level gets pinned at the trap energy level (Figure S12a). Also in this case, however, SPV decay times are lower than the ones measured in the experiment (Figure 8).

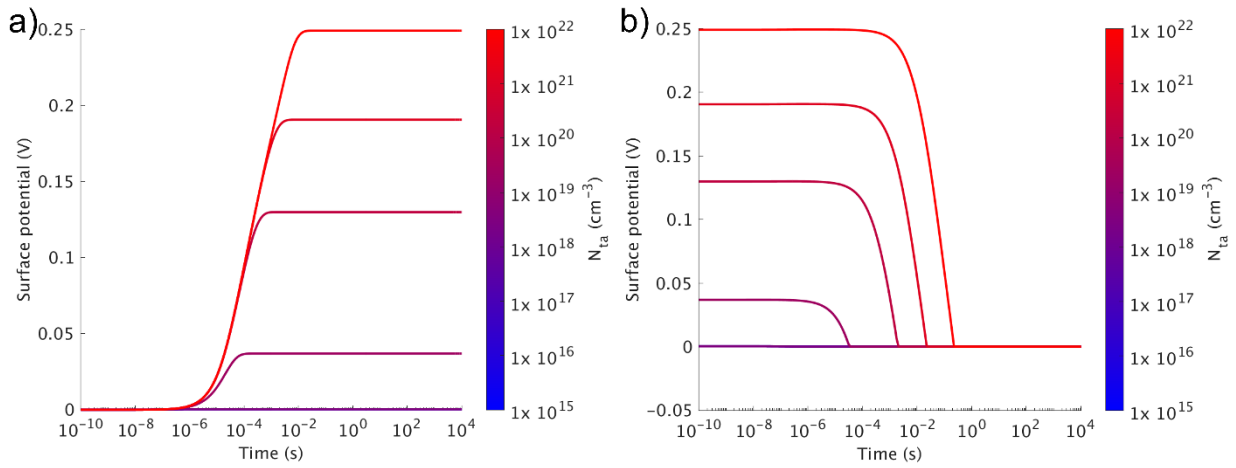

Figure 8: Perovskite - TiO_x transient SPV simulations for different values of acceptor trap density on a 5 nm layer thickness on the surface of $TiO_x(N_{ta})$, close to the interface with the perovskite: SPV rise (a) and decay (b) after illumination is switched off.

Contact work function

So far, the only buried heterojunction considered in our structures was the one at the perovskite-ETL or perovskite-HTL interface. The interface between the ETL (or HTL) and the back electrode was considered as neutral in the simulation, meaning that the work function of the ETL (or HTL) and that of the back electrode were taken as identical. In our experiment, the perovskite - TiO_x samples were deposited over fluorinated tin oxide (FTO). Such a transparent conductive oxide (TCO) can be modelled by the addition of a Schottky barrier at the back of the SCTL, by setting

the work function at the back contact to a value different from that of the SCTL. Thus, a space charge region can form inside the SCTL due to this WF difference.

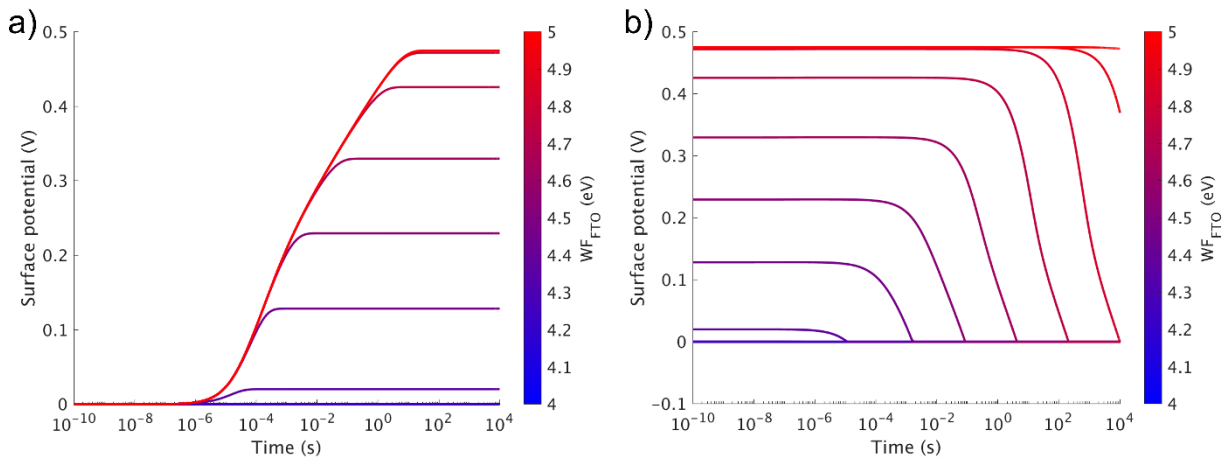

Figure 9: Perovskite - TiO_x transient SPV simulations for different values of the back contact work function (WF_{FTO}); build-up of SPV after illumination is switched on (a), and SPV decay after illumination is switched off (b).

With KPFM, we have measured the FTO WF to be 4.79 eV (Table 1). While the ITO and NiO_x WF were found to be nearly equal experimentally, suggesting the presence of an ohmic contact between the two, FTO and TiO_x WF values differ by about 400 meV, suggesting the presence of a buried Schottky contact.

Similarly to the perovskite – TiO_x affinity mismatch case discussed above, steady state conditions impose a net zero flux of electrons at the TiO_x – FTO interface. If the contact WF is increased beyond the TiO_x WF, a potential barrier forms between E_{C,TiO_x} and $E_{F,FTO}$. In order to overcome this barrier by thermionic emission, electrons accumulate in the FTO and thus a spatial separation of charge is obtained (Figure S12b). Thus, both the SPV magnitude and decay time increase with the contact WF, as shown in Figure 9. However, while the SPV decay times could be consistent with the experiment, the magnitude of the SPV is not (Figure S11).

3 |Conclusions

In this study, we combined experiments and modelling on specific perovskite-SCTL structures to discuss the equilibrium electrostatic potential distribution and the redistribution of charges upon illumination. On the one hand, our analysis conducted in equilibrium conditions supports the hypothesis of a low effective doping density, smaller than 10^{12} cm^{-3}, inside the perovskite. On the other hand, from drift-diffusion simulations for the bilayers under study, we showed that nearly intrinsic perovskite - moderately doped SCTL structures provide surface photovoltage values lower than 1 mV, while experimental values exceed hundreds of mV under the same continuous illumination conditions. Regarding the perovskite - TiO_x structure, we also excluded the effect of band offsets at the buried heterojunction due to decay time after switching off the illumination. Considering the presence of a TCO at the bottom of the structure, we studied the influence of the contact work function, which affects the SPV. Also in this case, however, varying uniquely this parameter does not allow to fit both the SPV magnitude and decay times.

We can suggest that the large timescale of the photovoltage decays of the perovskite-ETL samples could indicate the occurrence of reversible chemical reactions at the perovskite/SCTL interface, which were not considered in drift-diffusion simulations. Those reactions could be driven by the presence of a net charge inside the perovskite under illumination, due to the presence of the SCTLs and the TCO.

References:

[1] Park N-G, Perovskite solar cells: an emerging photovoltaic technology. Materials Today, 2015; 18, 2, 65-72.

[2] Ansari M-I-H, Qurashi A, Nazeeruddin M-K, Frontiers, opportunities, and challenges in perovskite solar cells: A critical review. J. Photochem. and Photobio. C: Photochemistry Reviews, 2018 ; 35, 1-24.

[3] Yin W-J, Shi T, and Yan Y, Unusual defect physics in $CH_3NH_3PbI_3$ perovskite solar cell absorber, Appl Phys Lett, 2014 ; 104, 063903.

[4] Meggiolaro D, Motti S-G, Mosconi E, Barker AJ, Ball J, Perini C-A-R, Deschler F, Petrozza A, and De Angelis F. Iodine chemistry determines the defect tolerance of lead-halide perovskites. Energy Environ. Sci., 2018; 11, 702-713.

[5] Motti S-G, Meggiolaro D, Martani S, Sorrentino R, Barker A-J, De Angelis F, Petrozza A, Defect activity in metal-halide perovskites. Adv. Mater. 2019; 31, 1901183.

[6] Jin H, Debroye E, Keshavarz M, Scheblykin I-G, Roeffaers M-B-J, Hofkens J, Steele J-A, It's a trap! On the nature of localised states and charge trapping in lead halide perovskites. Mater. Horiz., 2020 ; 7, 397-410.

[7] Euvrard J, Yan Y, and Mitzi, D. Electrical doping in halide perovskites. Chem. Commun., 2015 ; 51, 14917.

[8] Zhao L, Kerner R-A, Xiao Z, Lin Y-L, Lee K-M, Schwartz J, and Rand B-P, Redox chemistry dominates the degradation and decomposition of metal halide perovskite optoelectronic devices, ACS Energy Lett. 2016 ; 1, 3, 595–602.

[9] Almora O, Aranda C, Mas-Marzá E, and Garcia-Belmonte G, On Mott-Schottky analysis interpretation of capacitance measurements in organometal perovskite solar cells. Appl Phys Lett 2016 ; 109, 173903.

[10] Béchu S, Ralaiarisoa M, Etcheberry A, and Schulz P, Photoemission spectroscopy: photoemission spectroscopy characterization of halide perovskites Adv. Energy Mater. 2020 ; 10: 2070116.

[11] Barnea-Nehoshtan L, Kirmayer S, Edri E, Hodes G, and Cahen D, Surface photovoltage spectroscopy study of organo-lead perovskite solar cells, J. Phys Chem Lett, 2014 ; 5 (14), 2408-2413.

[12] Harwell J-R, Baikie T-K, Baikie I-D, Payne J-L, Ni C, Irvine J-T-S, Turnbull G-A, Samuel I-D-W. Probing the energy levels of perovskite solar cells via Kelvin probe and UV ambient pressure photoemission spectroscopy. Phys. Chem. Chem. Phys., 2016 ; 18, 19738-19745.

[13] Gallet T, Grabowski D, Kirchartz T, and Redinger A, Fermi-level pinning in methylammonium lead iodide perovskites, Nanoscale, 2019; 11, 16828-16836

[14] Schulz P, Whittaker-Brooks L-L, MacLeod B-A, Olson D-C, Loo, Yueh-Lin, Kahn A, Electronic level alignment in inverted organometal perovskite solar cells. Adv. Mater. Interfaces, 2015; 2: 1400532.

[15] Miller E-M, Zhao Y, Mercado C-C, Saha S-K, Luther J-M, Zhu K, Stevanović V, Perkinsa C-L, and Lagemaat J-V, Substrate-controlled band positions in $CH_3NH_3PbI_3$ perovskite films, Phys. Chem. Chem. Phys., 2014; 16, 22122-22130

[16] Zohar A., Kulbak M., Levine I., Hodes G., Kahn A., and Cahen D., What limits the open-circuit voltage of bromide perovskite-based solar cells?, ACS Energy Lett. 2019, 4, 1−7

[17] Dunfield S-P et al., Understanding carrier gradients and the role of charge selective contacts in lateral heterojunction all back-contact perovskite solar cells, Cell Reports Physical Science (accepted)

[18] Qiu L, He S, Ono L-K, Qi Y-B, Progress of surface science studies on ABX_3-based metal halide perovskite solar cells. Adv. Energy Mater. 2020 ; 10, 1902726.

[19] Wilken S, Parisi, and Borchert H, Role of oxygen adsorption in nanocrystalline ZnO interfacial layers for polymer–fullerene bulk heterojunction solar cells, J. Phys. Chem. C 2014 ; 118, 34, 19672–19682.

[20] Lu G, Linsebigler A, and Yates J-T , The adsorption and photodesorption of oxygen on the TiO2(110) surface, J. Chem Phys. 1995 ; 102, 4657-4662

[21] Wilson J-N, Frost J-M, Wallace S-K, and Walsh A, Dielectric and ferroic properties of metal halide perovskites, APL Materials. 2019 ; 7, 010901.